Journal of Power Sources 226 (2013) 313–319

Contents lists available at SciVerse ScienceDirect

Journal of Power Sources

journal homepage: www.elsevier.com/locate/jpowsour

# In-situ X-ray diffraction studies of lithium–sulfur batteries

Natalia A. Cañas [a,b,*], Steffen Wolf [a], Norbert Wagner [a], K. Andreas Friedrich [a,b]

[a] Institute of Technical Thermodynamics, German Aerospace Center, 70569 Stuttgart, Germany
[b] Institute for Thermodynamic and Thermal Engineering, University of Stuttgart, Germany

## HIGHLIGHTS

- ► Structural changes of lithium–sulfur batteries were studied by means of in-situ XRD.
- ► Dilithium sulfide was detected the first time at a depth of discharge of 60%.
- ► Sulfur recrystallizes with an orientated structure and lower crystallite size.
- ► Sulfur and dilithium sulfide were semi-quantitatively determined.

## ARTICLE INFO

*Article history:*
Received 2 August 2012
Received in revised form
9 October 2012
Accepted 29 October 2012
Available online 7 November 2012

*Keywords:*
Lithium–sulfur
Battery
In-situ
X-ray diffraction

## ABSTRACT

In order to optimize the cycling performance of lithium–sulfur (Li–S) batteries, it is highly important to understand the structural and morphological changes of the sulfur cathode under operating conditions. In this work, a suitable cell for in-situ X-ray diffraction (XRD) analysis was designed to study the structural modifications on the cathode of Li–S batteries during electrochemical cycling. As a result, the formation of reaction products during charging and discharging was monitored in operando. The formation of dilithium sulfide ($Li_2S$) and the recrystallization of sulfur during the first cycle could be identified. Moreover, these crystalline phases were semi-quantitatively determined by means of XRD analysis. Morphology changes of the cathode due to electrochemical cycling were characterized using scanning electron microscopy (SEM).

© 2012 Elsevier B.V. All rights reserved.

## 1. Introduction

Due to its high theoretical capacity (1672 mAh $g_{sulfur}^{-1}$) and energy density (2500 Wh $kg^{-1}$), lithium–sulfur batteries have attracted widespread attention in the battery research community. Further advantages are the low cost and non-toxicity of sulfur. Nevertheless, a known problem of lithium–sulfur batteries is the gradual decrease of discharge capacity during cycling. This is mainly caused by the low electrical conductivity of sulfur and dilithium sulfide, and the formation of soluble polysulfides in the electrolyte. In order to react electrochemically, sulfur has to be in contact with an electrical conductive material (like carbon black, graphite or carbon nanotubes). The morphology of the cathode can change upon cycling and the formerly well-dispersed sulfur can aggregate and become isolated for further reaction. Furthermore, polysulfides of high order ($Li_2S_n$ with $4 \leq n \leq 8$) dissolve in the electrolyte and can diffuse to the anode and react directly with lithium metal. This so-called shuttle mechanism causes irreversible loss of sulfur [1–3]. The polysulfide discharge product, $Li_2S$, is insoluble in the electrolyte and can precipitate on the surface of electrodes, acting as an insulator and avoiding further electrochemical reactions.

In order to understand the degradation mechanisms of this battery, the application of in-situ techniques is necessary. An important characterization method to follow structural and composition changes in a battery during cycling is the analysis by means of X-ray diffraction. In the past, in-situ XRD experiments were already performed successfully on lithium-ion batteries, for example in Refs. [4–10]. So far, however, there has been little application of this method in Li–S batteries [11,12]. In a recent research [12], the formation of the discharge product $Li_2S$ was not detected in operando conditions. In contradiction to these results, we find, that dilithium sulfide does build up during the first discharge cycle. It is important to highlight that dilithium sulfide is a difficult substance to investigate, because it hydrolyzes easily in air, producing $H_2S$ and LiOH. Probable reasons why $Li_2S$ has not

* Corresponding author. Institute of Technical Thermodynamics, German Aerospace Center, 70569 Stuttgart, Germany. Tel.: +49 0711 6862 576; fax: +49 0711 6862 474.
*E-mail address:* natalia.canas@dlr.de (N.A. Cañas).

0378-7753/$ – see front matter © 2012 Elsevier B.V. All rights reserved.
http://dx.doi.org/10.1016/j.jpowsour.2012.10.092

been detected before are I) the in-situ cell is not airtight, II) the discharge capacity of the cell is too low, $Li_2S$ does not precipitate and only soluble polysulfides are present at discharge state or III) the penetration depth of the X-ray is not high enough and the structural information is only from a deeper region of the bulk cathode material, giving no information from the interface cathode/separator, where probably the main quantity of $Li_2S$ is present.

In this paper, the reactions of crystalline phases in the Li–S battery were monitored for the discharging and charging process by means of in-situ XRD. The formation of dilithium sulfide and the recrystallization of sulfur have been identified. In addition, this work is complemented with semi-quantitative analysis of the species and SEM characterization of the cathode surface.

## 2. Experimental

### 2.1. Cathode preparation

The cathodes consisted of 50 wt.% sulfur (99.5%, Alfa Aesar), 40 wt.% Super P conductive carbon black (99%, Alfa Aesar) and 10 wt.% polyvinylidene fluoride (PVDF, Alfa Aesar).

First, sulfur and carbon black were mixed for 12 h in a tumbling mixer. PVDF was dissolved in a 50/50 vol.% mixture of dimethyl sulfoxide (DMSO, 99.9%, Sigma Aldrich) and ethanol (99.5%, VWR). All chemical compounds were finally mixed together for 6 h.

The suspension was sprayed by use of an air-atomizing external mixing nozzle (LECHLER GmbH) controlled by a 3D axis robot. Each cathode was prepared by spraying four layers over a 6 μm thick aluminum collector. Between each spraying, the cathode was dried in an oven at 60 °C. The drying step improves the adherence of the cathode coating on the aluminum collector and the homogeneity of the layers. The thickness of the cathode layer, without substrate, varied between 15 μm and 20 μm.

### 2.2. In-situ cell

The in-situ cell consists of two holed aluminum plates, the cathode plate with a thin aluminum window and the anode plate. The aluminum window is fixed onto the cathode plate with a conductive epoxy. Each plate acts as electrode collector and can be connected directly to the potentiometer inserting banana jacks in the hole located in each plate of the cell. A plastic tube is placed in the middle of the cell to insulate electrically the battery from the interior walls of the cell. In order to seal the cell airtight, a 0.75 mm thick polymer gasket is positioned between the two plates. Additionally, this avoids an internal short circuit between both electrode plates. A metal spring inside the cell applies mechanical pressure of the stack (see Fig. 1, components 5–8) against the Al-window. An exploded illustration of the cell composition is shown in Fig. 1.

### 2.3. Assembling of the cell

The battery was assembled in a Glove Box under Argon atmosphere. The 1.5 mm thick lithium anode (99.9%, Sigma Aldrich) was placed on an aluminum disk over the spring. The separator, a 25 μm thick polypropylene microporous membrane (Celgard 2500), was set on top of the anode and soaked with 14 μL electrolyte, 1 M $LiPF_6$ (99.99%, Sigma Aldrich) in tetraethylene glycol dimethyl ether (TEGDME, 99.9%, Sigma Aldrich). The cathode was placed on the separator. The cell-stack was positioned in the in-situ cell and this was finally closed with plastic screws. The diameter of the lithium foil and cathode was 10 mm, while the separator diameter was 2 mm larger dimensioned to avoid short circuit. We used a thin Al-foil of 6 μm thick that allows us to obtain information until the separator surface. Fig. 8, Ia, b shows SEM pictures of the cathode before cycling. It can be seen that the sulfur particles were covered with the carbon black nanoparticles.

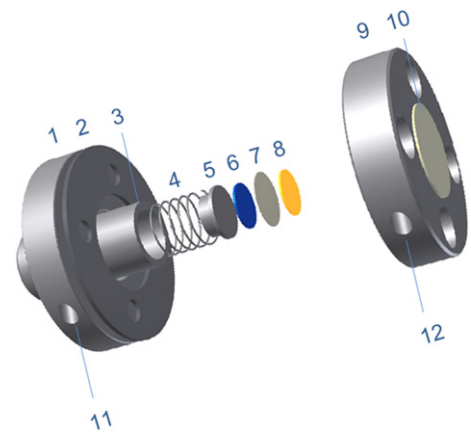


**Fig. 1.** Exploded illustration of the in-situ XRD cell. 1) Anode plate, 2) polymer gasket, 3) insulator plastic tube, 4) spring, 5) Al-anode collector, 6) anode, 7) separator, 8) cathode, 9) cathode plate, 10) Al-window and 11–12) holes for connecting the banana jacks.

### 2.4. Electrochemical cycling, X-ray diffraction and scanning electron microscopy

The cycling performance of the battery was investigated by use of a Zahner® IM6 electrochemical workstation, with the battery measurement software Zahner® Thales [13]. The charge–discharge procedure was carried out in galvanostatic mode at a current density of 300 mA $g_{sulfur}^{-1}$ in a voltage range between 2.8 V and 1.5 V. Once the charge end voltage of 2.8 V was reached, a potentiostatic period followed for 15 min before starting the next cycle.

X-ray diffractograms were recorded with an X-ray diffractometer, D8 Discover GADDS, equipped with a VÅNTEC-2000 area detector. Exposures were made in reflexion mode with a tuned monochromatic and parallel X-ray beam (Cu-$K_\alpha$), with a tube collimator aperture of 1 mm. The accelerating voltage was 45 kV and the tube current was 0.650 mA. Each diffraction pattern was measured in four frames with a step size of 23°, starting with $\theta_1 = \theta_2 = 12°$ (Bragg–Brentano condition). The exposure time for each frame was 180 s.

Twelve minutes were required to record each in-situ XRD pattern. The electrochemical testing of the cell was not stopped neither during charging nor discharging. For this reason, the XRD pattern represents averaged values of the reflected X-ray during the exposure time.

The morphological changes on the cathode surface were observed in SEM (Zeiss ULTRA plus with Charge Compensation). The accelerating voltage was 1 kV and the secondary electron detector was used.

## 3. Results and discussion

### 3.1. Discharge cycle

Fig. 2 shows the X-ray patterns measured at different depth of discharge (DOD, %) during the first galvanostatic discharge. Thereby, only the range of interest of the diffraction patterns ($2\theta = 20°–35°$) is shown. The Bragg peaks of sulfur can be clearly detected in the first spectrum (Power Diffraction File [14], PDF, number: 00-008-0247). The structure of sulfur is orthorhombic face centered, which is the stable modification of sulfur below 96 °C

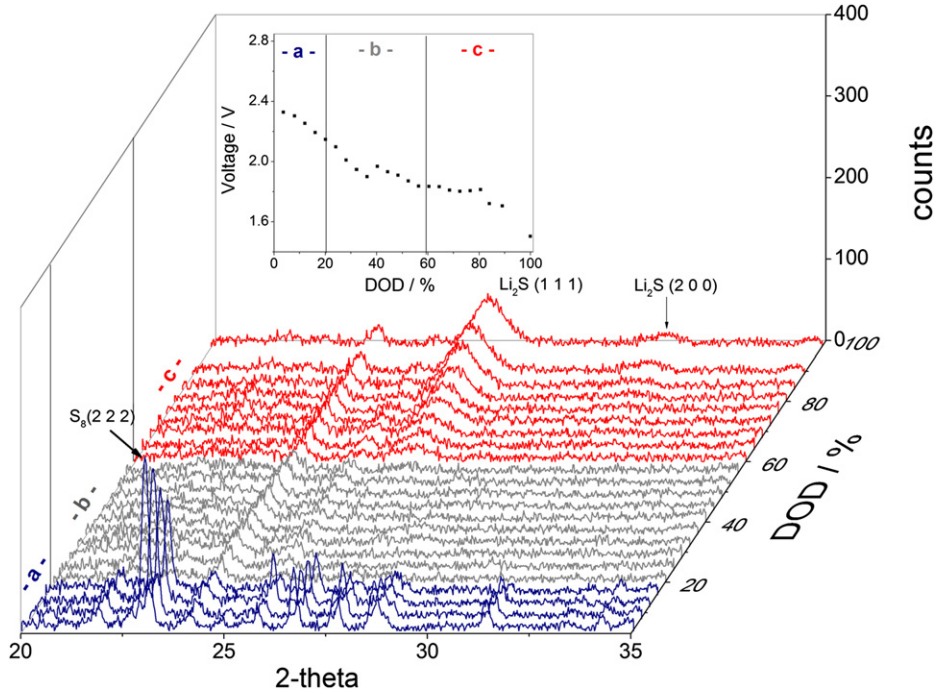


**Fig. 2.** In-situ X-ray diffraction data collected during discharging of Li–S battery at a rate of 300 mA $g^{-1}$. Three different regions are shown: a) reaction of sulfur to high order polysulfides (blue), b) reactions of high order polysulfides (gray) and c) formation of $Li_2S$ (red). The discharge curve is shown on the top. The average discharge capacity is 1276 mAh $g^{-1}_{sulfur}$. (For interpretation of the references to color in this figure legend, the reader is referred to the web version of this article.)

[15]. The reflexion at $2\theta = 24°$ does not correspond to sulfur but to the separator material. This is important because it means that the cathode was radiated through its whole thickness.

According to these measurements, the corresponding discharge curve in Fig. 2 can be divided in three periods: a) from 0 to 20% DOD, where crystalline sulfur is detected and its peak intensities are gradually decreasing, b) from 20 to 60% DOD, where no crystalline phase is present and c) from 60 to 100% DOD, where the progressive formation of $Li_2S$ can be observed. The suggested reaction mechanism is described according with Refs. [16,17], see reactions (1)–(7). According to our knowledge, the formation of $Li_2S_2$ (s) has not been yet detected in Li–S batteries, thus we do not

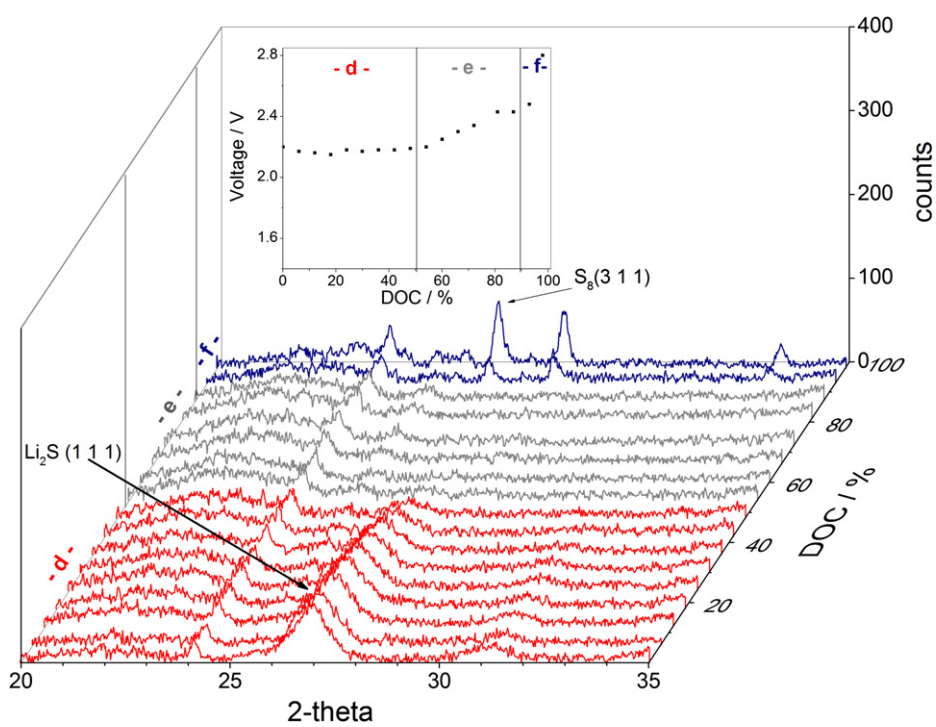


**Fig. 3.** In-situ X-ray diffraction data collected during charging of Li–S battery at a rate of 300 mA $g^{-1}$. Three different regions are shown: d) reaction of $Li_2S$ (blue), e) reactions of high order polysulfides (gray) and f) formation of sulfur (red). The charge curve is shown on the top. Average charge capacity: 1283 mAh $g^{-1}_{sulfur}$. (For interpretation of the references to color in this figure legend, the reader is referred to the web version of this article.)

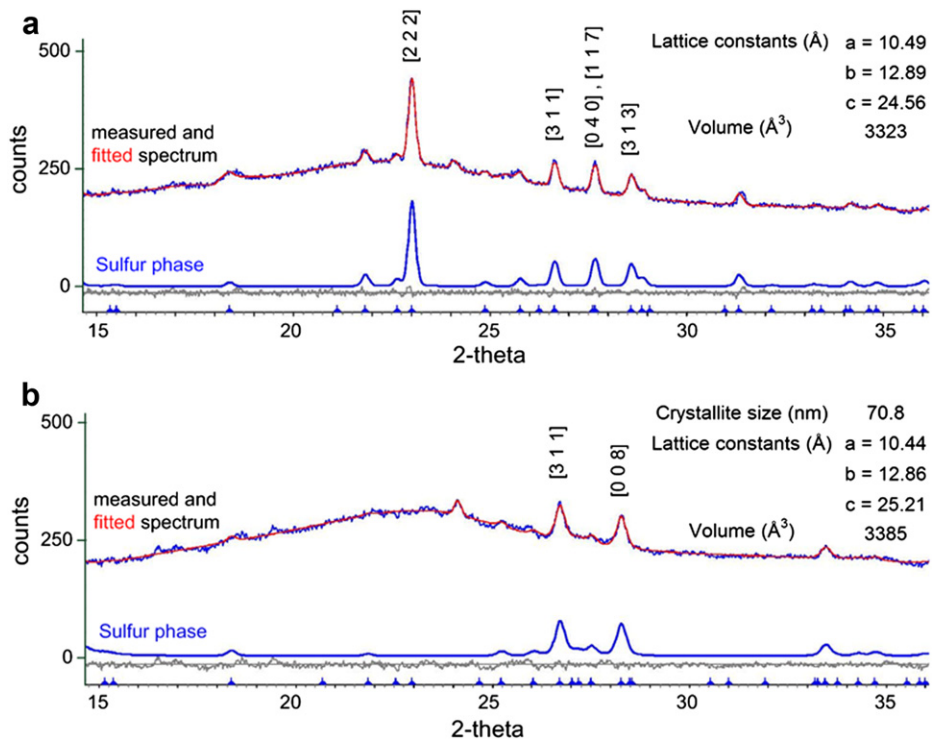


**Fig. 4.** Results of Rietveld refinement for X-ray pattern of sulfur after charging.

considered the formation of crystalline $Li_2S_2$ as a reaction step. During stage (a), the upper plateau region; sulfur successively dissolves (1) and starts to reduce to high order polysulfides (2–4). At the beginning of the discharge step, sulfur is mostly in the $S_{8(s)}$ crystalline phase, due to its low solubility in TEGDME (0.94 wt.%) [18]. Around 30% of the initial sulfur should be dissolved in the electrolyte, considering the dissolution formula in Ref. [18]. As the discharge proceeds, the dissolved $S_{8(l)}$ in the electrolyte is consumed by the electrochemical reaction (2), the concentration of $S_{8(l)}$ decreases, enhancing further dissolution of crystalline sulfur into the liquid phase [16].

$$S_{8(s)} \rightleftarrows S_{8(l)} \tag{1}$$

$$2Li + S_{8(l)} \rightleftarrows 2Li^{+1} + S_{8(l)}{}^{-2} \tag{2}$$

$$2Li + \tfrac{3}{4}S_{8(l)}{}^{-2} \rightleftarrows 2Li^{+1} + S_{6(l)}{}^{-2} \tag{3}$$

$$2Li + \tfrac{2}{3}S_{6(l)}{}^{-2} \rightleftarrows 2Li^{+1} + S_{4(l)}{}^{-2} \tag{4}$$

$$2Li + S_{4(l)}{}^{-2} \rightleftarrows 2Li^{+1} + 2S_{2(l)}{}^{-2} \tag{5}$$

$$2Li + \tfrac{1}{2}S_{2(l)}{}^{-2} \rightleftarrows 2Li^{+1} + S_{(l)}{}^{-2} \tag{6}$$

$$2Li^{+1} + S_{(l)}{}^{-2} \rightleftarrows Li_2S_{(s)}\downarrow \tag{7}$$

From 20% until 60% DOD no diffraction peaks can be observed. Due to the dissolution of sulfur and the formation of high order polysulfides (2–4), the diffraction peaks of sulfur abruptly disappear at 20% DOD. The concentrations of $S_{8(l)}$, $S_{8(l)}{}^{-2}$, $S_{6(l)}{}^{-2}$ $S_{4(l)}{}^{-2}$ decrease and the reduction of the polysulfides down to $S_{(l)}{}^{-2}$ starts (5–6).

From 60% DOD on, $Li_2S$ diffractions peaks can be detected for the first time and their intensity increased continuously until the end of the discharge step. $Li_2S$ has a cubic face centered structure (PDF

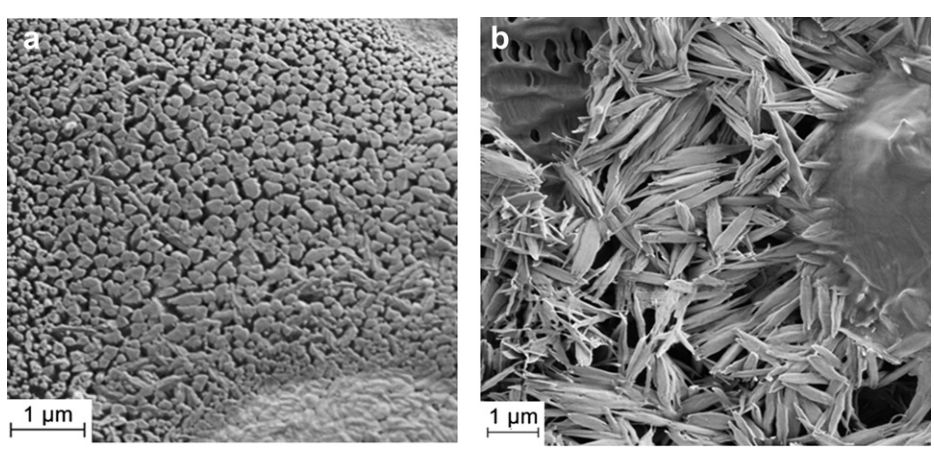


**Fig. 5.** SEM micrographs of a separator section viewed from the cathode side.

number: 00-023-0369). $Li_2S$ peaks are broad, e.g. $Li_2S$ (111)-peak has a full width at high maximum (FWHM) of 0.904° ± 0.027°. Broad peaks reveal in this case that $Li_2S$ crystallites are nano-sized and the results of the fit with Topas confirm a crystallite size of 6.3 ± 0.4 μm at 100% DOD. Due to this peak shape, the analysis of low concentrations of $Li_2S$ is difficult, because these broad peaks may not be distinguishable from the background of the spectrum and cannot be quantify. For this reason, the precipitation of $Li_2S_{(s)}$ (7) may start at a lower rate than 60% DOD, even though no crystalline phase has been detected by means of XRD.

According with Ryu et al. [20], sulfur reacts completely to $Li_2S_n$ at the upper plateau in electrodes discharged at low current densities (100–400 mA $g^{-1}_{sulfur}$). Following, dissolved polysulfides react partially to $Li_2S$ at the second discharge plateau.

Nelson et al. [12] carried out in-situ XRD measurements on Li–S batteries at similar current density. Similar to our work, they found crystalline sulfur at the beginning of the discharge cycle (until ~23% DOD). Nevertheless, at the end of discharge no $Li_2S$ was detected in-situ. Taking into account the low discharge capacity (~750 mAh $g^{-1}_{sulfur}$) of their battery, the formation of $Li_2S$ may not have been detected because the reduction of sulfur was not completed and $Li_2S$ did not precipitate.

### 3.2. Charge cycle

The X-ray patterns of the charging step are shown in Fig. 3. Once the battery starts to charge, $Li_2S$ reacts to high order polysulfides. The progress of the reaction can be followed with the decrease of area under the main reflexion peak (111) of $Li_2S$. It diminishes continually toward zero up to a 50% depth of charge (DOC). The reverse reactions (7–6) may be the main contribution during this stage. In the range between 50 and 95% DOC no crystalline $Li_2S$ was found. High order polysulfides are formed and dissolved in the electrolyte, according to reverse reactions: (4–2). New Bragg peaks can be observed after 95% DOC due to the formation of crystalline sulfur. However, the (222) reflexion of $S_8$, identified before cycling, cannot be detected after recrystallization. The crystal structure of sulfur formed after the first charging could not be linked to any previously measured sulfur structure from the PDF database [14]. Therefore, the Diffracplus Topas software [19] was used to fit the results with the orthorhombic structure of sulfur (space group = 70). The lattice parameters and particle size were considered as free variables for the fitting. Fig. 4 illustrates the results of the refinement of the sulfur structure.

The orientation of sulfur particles is probably due to epitaxial growth of sulfur crystallites on the carbon substructure. The carbon paticles may act as nucleation centers and the deposited layer show preferential crystallographic orientations with respect to the substrate. The recrystallization of sulfur at the end of the first discharge was also detected by Ref. [12]. They observed some

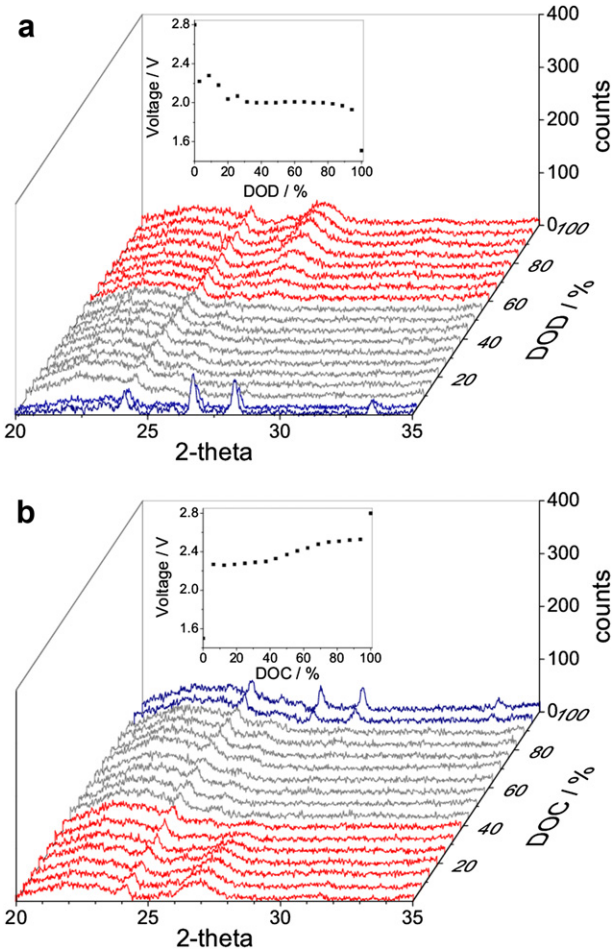


**Fig. 6.** In-situ X-ray diffraction data collected during 2. discharge (a) and 2. charge (b) of Li–S battery at a rate of 300 mA $g^{-1}$.

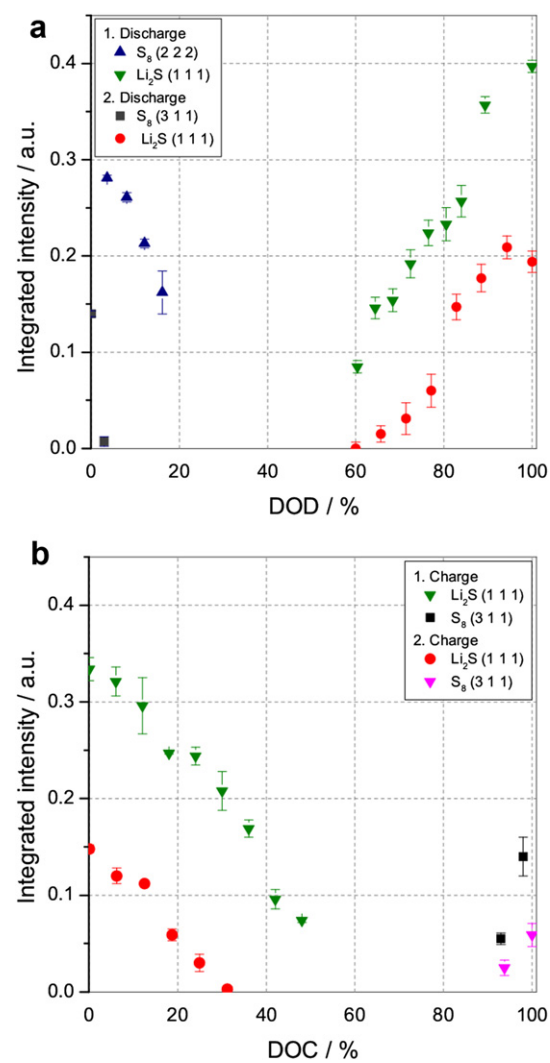


**Fig. 7.** Semi-quantitative X-ray analysis for the first two discharge (a) and charge cycles (b) of a Li–S battery.

changes in the position of sulfur Bragg peaks, which was interpreted as an anisotropic orientation of $S_8$ particles.

According to the changes in the reflexion positions and intensities, recrystallization of sulfur may occur by a reorientation of the particles. This has also been observed by ex-situ measurements by SEM. Fig. 5 shows two different sections of the separator surface viewed from the cathode side after cycling and cell dissembling. In Fig. 5a, some amount of sulfur crystallized on the separator surface (cathode side) and the particles exhibit a preferred orientation. The particles are shaped like "sulfur needles" aligned perpendicular to the separator surface. In some areas, like in Fig. 5b, the sulfur particles are disordered, probably due to the dissembling of the cell. However, this area is shown to clarifying the "needle" structure. The particle size is not larger than 2 μm. Some amorphous material can be seen in the right side of the picture.

### 3.3. Second cycle and semi-quantitative analysis of crystalline species

In Fig. 6 the spectra for the second cycle are shown. The crystalline products $S_8$ and $Li_2S$ react completely, but the intensity of the peaks decreases at the end of discharge and charge. The formation of an amorphous phase can be clearly seen at angles of 20°–24° during the second charge (Fig. 6b).

To semi-quantify the reactant and product species, the integrated intensity of the Bragg reflexions of sulfur (222) (311) and dilithium sulfide (111) was calculated at different DOD and DOC. The integrated intensity is the area under the peaks and it is directly proportional to the volume of the crystallites in the sample. In the case of sulfur, the (222) reflexion was chosen for the peak integration during discharging and the (311) reflexion during charging. Unfortunately, due to the change of location of the Bragg reflexion of sulfur in the XRD pattern after charging, it is not possible to estimate the quantity of sulfur that has recrystallized after the first charge cycle. The dissolution and reaction of sulfur is only observed in the first 20% DOD of the discharge cycle. The formation of dilithium sulfide is slower and can be detected in the last 60% DOD of the discharge time. During charging, the reaction of $Li_2S$ is slower compared with the recrystallization rate of sulfur. By the second discharge, almost 50% less crystalline $Li_2S$ is formed compared with the first discharge. At the end of the second charge, the peaks of sulfur appear at the same positions, indicating a similar orientation of the particles as the one after the first charge (Fig. 7).

### 3.4. Morphological changes during cycling

Fig. 8 illustrates the morphological changes on the cathode surface during discharging. In Fig. 8, Ia, the sulfur particles are covered with carbon black nanoparticles, although some of them are not totally enclosed (Fig. 8, Ib). However, after 20% DOD (Fig. 8, II) no particles of sulfur are observed any longer and some cavities, probably generated after dissolution and reaction of sulfur, can be identified. In the middle of the second discharge plateau (Fig. 8, III) the cathode is partially covered by a solid layer. Small crystallites homogeneously distributed on the surface can be observed in the non-covered area of the cathode. The images of the fully discharged cathode (Fig. 8, IV) exhibit a completely covered surface.

Due to the fact that all the samples were measured ex-situ, it is important to emphasize that this layer or crystallites may be a result of the reaction of polysulfides and electrolyte compounds with air after dissembling the cell. However, by ex-situ XRD measurements of the cathodes (Fig. 8, II–IV), no crystalline components could be identified. The reason for this might be the insufficient quantity of these unknown compounds in the sample.

The SEM pictures of the cathode surface during charging are shown in Fig. 9. In the discharge state (Fig. 9, IV), the cathode is

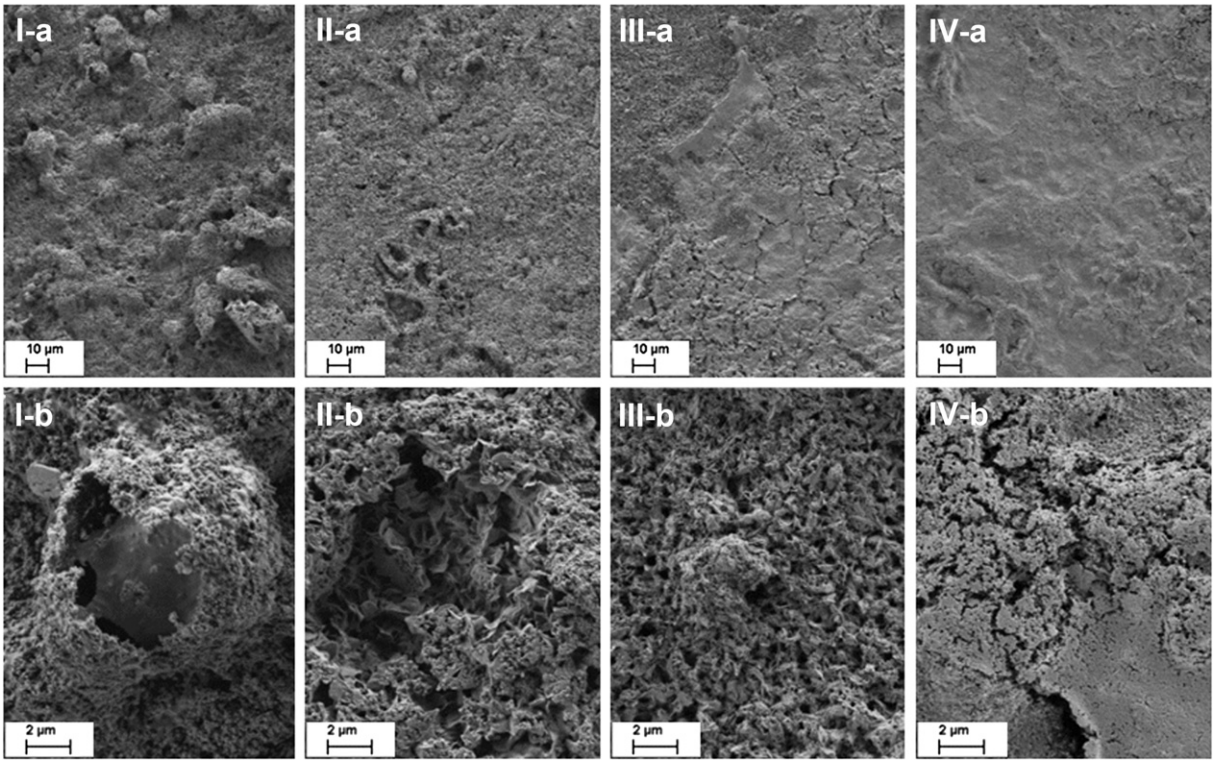


**Fig. 8.** Ex-situ SEM micrographs of the cathode surface during the first discharge. Picture magnifications: 300× (a) and 3000× (b). I) Before cycling; II) at the end of the first discharge plateau, 20% DOD; III) at the second discharge plateau, 40% DOD; IV) discharged, 100% DOD, 1.5 V. Average discharge capacity: 1276 mAh $g_{sulfur}^{-1}$.

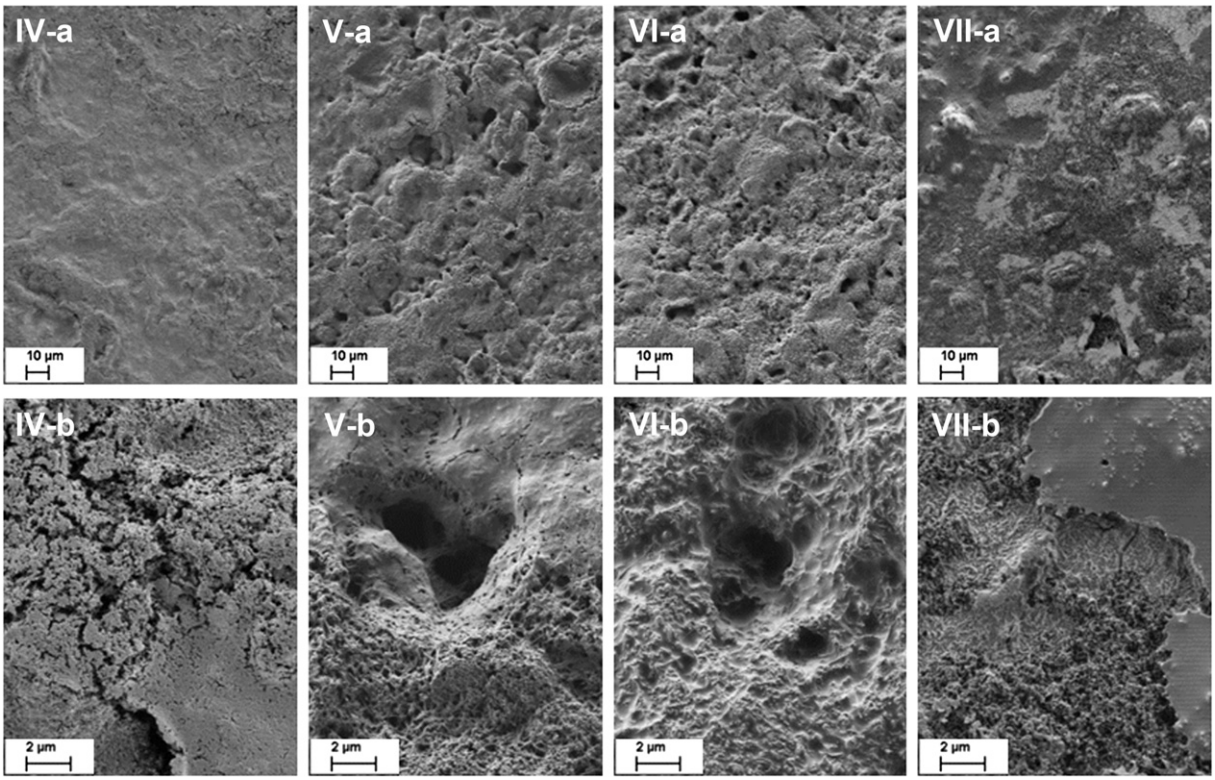


**Fig. 9.** Ex-situ SEM micrographs of the cathode surface during the first charge. Picture magnifications: 300× (a) and 3000× (b). V) At the first plateau, 40% DOC, VI) at the second discharge plateau, 80% DOC, VII) after the first charge, 100% DOC. The average charge capacity is 1283 mAh $g_{sulfur}^{-1}$.

covered by a layer which gradually vanishes during charging. Like it can be seen in Fig. 9, V, after the battery was charged until a 40% DOC, the cathode surface changes revealing cavities, although it is still partially covered by the layer observed in Fig. 9, IV. At the beginning of the second charging plateau, the surface seems to be uncovered and more cavities are present (Fig. 9, VI). Finally, once the battery is completely charged, the cavities on the cathode surface are filled with sulfur (Fig. 9, VII) and the surface is partially covered with, what seems to be, a thin amorphous layer (see right section of Fig. 9, VIIb).

## 4. Conclusion

In this work, the cathode of lithium–sulfur battery was investigated by means of in-situ XRD. We demonstrated that at a discharge rate of 300 mA $g^{-1}$ sulfur reduces consecutively during the first discharge to $Li_2S$. The formation of $Li_2S$ was observed for the first time at a depth of discharge of 60% in the second discharge plateau at 1.8 V. During the charge cycle, $Li_2S$ reacts entirely and sulfur recrystallizes with a different orientated structure and smaller particle size. The crystalline reaction products ($S_8$ and $Li_2S$) were semi-quantitatively determined using the relative integrated intensity measured by means of XRD. Finally, SEM pictures showed the morphological changes of cathode surface during cycling.

This work wants to emphasize the importance of in-situ studies to understand the structural modifications of Li–S batteries and the influence in the degradation behavior during cycling.

## Acknowledgments

The authors want to acknowledge the financial support for the instrumentation from the Federal Ministry of Education and Research within the project “Elektrochemie für Elektromobilität – Verbund Süd-03KP801” and the State Ministry for Research and Education of Baden-Württemberg as well as Brennstoffzelle + Batterie-Allianz Baden-Württemberg (BBA-BW) and e-mobil BW.

Werner Seybold is acknowledged for helping with the building of the in-situ cell and Ina Plock for the SEM micrographs.

## Appendix A. Supplementary data

Supplementary data associated with this article can be found, in the online version, at http://dx.doi.org/10.1016/j.jpowsour.2012.10.092.

## References

[1] Y.V. Mikhaylik, J.R. Akridge, J. Electrochem. Soc. 151 (2004) A1969–A1976.
[2] V.S. Kolosnitsyn, E.V. Karaseva, Russ. J. Electrochem. 44 (2008) 506–509.
[3] J.R. Akridge, Y.V. Mikhaylik, N. White, Solid State Ionics 175 (2004) 243–245.
[4] J.R. Dahn, M.A. Py, R.R. Haering, Can. J. Phys. 60 (1982) 307–313.
[5] B. Gustafsson, J. Thomas, Electrochim. Acta 37 (1992) 1639–1643.
[6] O. Bergström, T. Gustafsson, J. Thomas, J. Appl. Crystallogr. 31 (1998) 103–105.
[7] M. Balasubramanian, X. Sun, X.Q. Yang, J. McBreen, J. Power Sources 92 (2001) 1–8.
[8] G.A. Roberts, K.D. Stewart, Rev. Sci. Instrum. 75 (2004) 1251.
[9] S. Misra, N.X. Ji, K.T. Lee, L.F. Nazar, Nat. Mater. 8 (2009) 500–506.
[10] S. Misra, N. Liu, J. Nelson, S. Sae Hong, Y. Cui, ACS Nano 6 (2012) 5465–5473.
[11] J. Hassouna, Y.-K. Sunb, B. Scrosati, J. Power Sources 196 (2011) 343–348.
[12] J. Nelson, S. Misra, Y. Yang, A. Jackson, Y. Liu, H. Wang, H. Dai, J.C. Andrews, Y. Cui, M. Toney, J. Am. Chem. Soc. 134 (2012) 6337–6343.
[13] ZAHNER-Elektrik GmbH & Co.KG, Thales Software, Germany.
[14] International Centre for Diffraction Data (ICCD), PDF-2 Release 2009, USA.
[15] B.E. Warren, J.T. Burwell, J. Chem. Phys. 3 (1935) 6–8.
[16] K. Kumaresan, Y. Mikhaylik, R.E. White, J. Electrochem. Soc. 155 (2008) A576.
[17] J.P. Neidhardt, D.N. Fronczek, T. Jahnke, T. Danner, B. Horstmann, W.G. Bessler, J. Electrochem. Soc. 159 (2012) A1528–A1542.
[18] S.F. Sciamanna, S. Lynn, Ind. Eng. Chem. Res. 27 (1998) 485–491.
[19] Bruker AXS, Topas Version 4.2, 1999, 2009, Germany.
[20] H.S. Ryu, Z. Guo, H.J. Ahn, G.B. Cho, H. Liu, J. Power Sources 189 (2009) 1179–1183.